ACS APPLIED MATERIALS & INTERFACES

RESEARCH ARTICLE

www.acsami.org

# Nanoforest $Nb_2O_5$ Photoanodes for Dye-Sensitized Solar Cells by Pulsed Laser Deposition

Rudresh Ghosh,[†,‡] M. Kyle Brennaman,[§] Tim Uher,[†] Myoung-Ryul Ok,[⊥] Edward T. Samulski,[§] L.E. McNeil,[†] Thomas J. Meyer,[§] and Rene Lopez*[,†,‡]

[†]Department of Physics and Astronomy, [§]Department of Chemistry, [‡]Institute for Advanced Materials, and [⊥]Curriculum in Applied Sciences and Engineering, University of North Carolina at Chapel Hill, Chapel Hill, North Carolina 27599-3290, United States

**ABSTRACT:** Vertically aligned bundles of $Nb_2O_5$ nanocrystals were fabricated by pulsed laser deposition (PLD) and tested as a photoanode material in dye-sensitized solar cells (DSSC). They were characterized using scanning and transmission electron microscopies, optical absorption spectroscopy (UV−vis), and incident-photon-to-current efficiency (IPCE) experiments. The background gas composition and the thickness of the films were varied to determine the influence of those parameters in the photoanode behavior. An optimal background pressure of oxygen during deposition was found to produce a photoanode structure that both achieves high dye loading and enhanced photoelectrochemical performance. For optimal structures, IPCE values up to 40% and APCE values around 90% were obtained with the $N_3$ dye and $I_3^-/I^-$ couple in acetonitrile with open circuit voltage of 0.71 V and 2.41% power conversion efficiency.

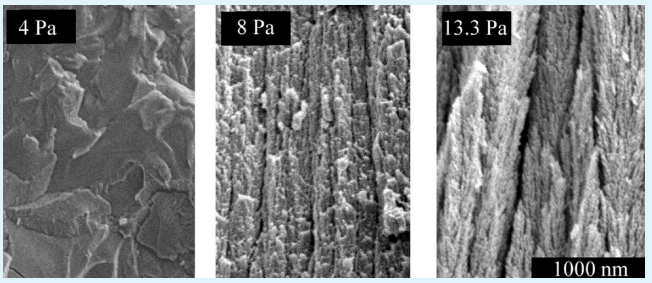


**KEYWORDS:** niobium oxide, dye -sensitized solar cell, pulsed laser deposition, IPCE

## 1. INTRODUCTION

The need for sustainable power generation has stimulated research in photovoltaic and photoelectrochemical materials and structures, with greater emphasis on a balance between cost and performance. Currently the majority of deployed solar cells are made of crystalline silicon (c-Si) with an efficiency of approximately 15−20%; however, the costs incurred to fabricate those cells will probably not allow them to become a large component of the future energy portfolio. For solar technologies to be more than niche products, cell efficiency must be improved in systems that are based on abundant materials and involve low-cost of fabrication.[1] In 1991 dye-sensitized nanocrystalline $TiO_2$ solar cells (DSSCs) based on a fast regenerative photoelectrochemical process were first reported by Grätzel et al.[2] with 7.1% efficiency. Today, the power conversion efficiency of DSSC cells has been improved to 11.5%,[3] and large-scale DSSCs have begun to be commercialized. Their minimal environmental impact, low cost, short energy payback time, and good performance in most operating conditions are important features that make DSSCs a very promising energy technology. Nevertheless, the efficiencies of current devices are still 55−70% of the theoretical maximum.[4] DSSCs are fabricated using a sensitized photoanode, a platinum counter electrode, and a redox electrolyte, e.g., $I_{3-}/I^-$ operating regeneratively.[5,6] The photoanode is composed of a few-micrometers-thick film of interconnected metal oxide semiconductor nanoparticles coated with light-harvesting molecules, typically Ru(II) polypyridyl complexes, and deposited on a transparent conductive substrate. The most successful DSSCs have photoanodes made with nanocrystalline $TiO_2$. However, the transport of charge within the disordered $TiO_2$ nanostructure is dominated by diffusion[7] (instead of drift), requiring $1 \times 10^3$ to $1 \times 10^6$ [8,9] interparticle hopping steps for a charge carrier to traverse a layer a few micrometers thick. This is a consequence of the high dielectric constant of the medium and the small nanocrystal size, such that photogenerated charge carriers are screened from significant electric fields by the electrolyte, limiting the effective electron transport length to about ∼10 $\mu$m.[10]

This limitation has prompted the investigation of low dimensional structures such as wires, rods, tubes, etc., with the goal of improving charge diffusion with a more direct transport.[11,12] Recently Gratzel et al.[13] introduced a novel photoanode with a nanoscale structure that resembled a forest, fabricated by pulsed laser deposition (PLD) under relatively high background gas pressures. This new nanostructure, which they named "nanoforest", replaces the traditional random nanoparticle oxide network by vertically aligned bundles of $TiO_2$ oxide nanocrystals. Gratzel had speculated earlier that a structure combining the high surface area of nanoparticles with the electron transport directionality of vertical rods would be optimal for DSSCs.[14] In addition to optimizing the oxide nanostructure, the use of other metal oxides and/or doped materials with higher conduction band energies[15,16] should, in principle, allow further improvement in DSSCs. This is because as long as the dye can inject electrons, enhancing the conduction band level relative to the electrolyte redox/oxidation level results in higher internal photovoltage.[7] $Nb_2O_5$ is an

**Received:** June 22, 2011
**Accepted:** September 15, 2011
**Published:** September 15, 2011

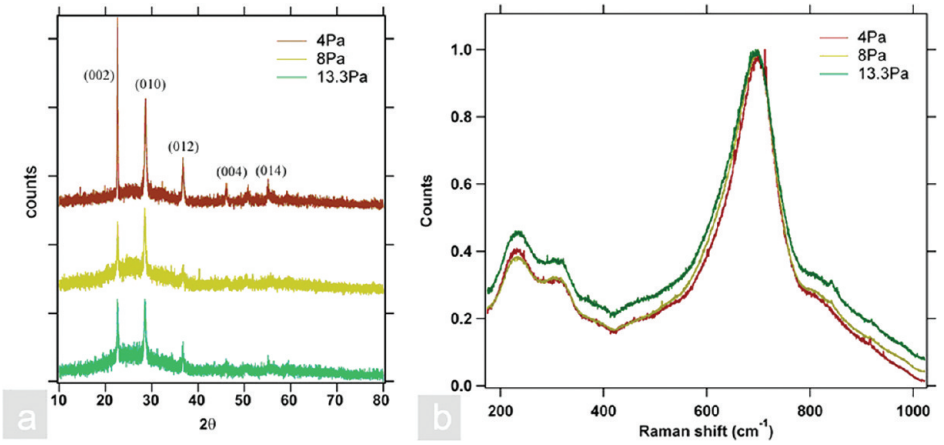


**Figure 1.** X-ray diffraction and normalized Raman spectra obtained for films made at different background oxygen pressures. The position and peak heights show the crystal structure (orthorhombic $Nb_2O_5$) of the different films grown under different gas pressures and post annealed at 500 C.

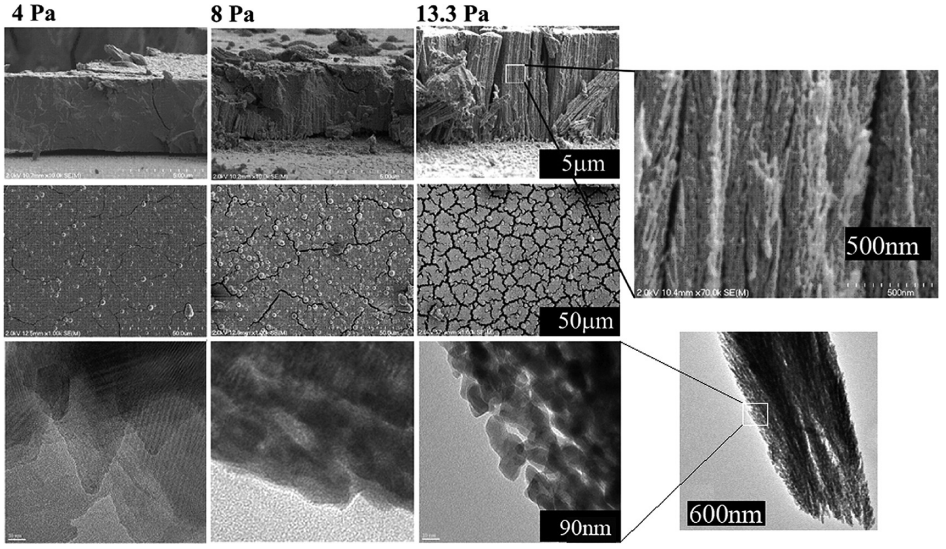


**Figure 2.** Top and cross-sectional views (SEM and TEM) of $Nb_2O_5$ films deposited at different background oxygen pressures.

example of one such n-type transition metal oxide with a higher conduction band edge than $TiO_2$.[17] Jose et al.[15] have recently studied the suitability of this and other metal oxides as photoanodes for DSSCs. They suggest that for a chemically stable binary oxide like $Nb_2O_5$, with a higher conduction band edge than $TiO_2$, it could be possible to attain higher open circuit voltages ($V_{oc}$) and photoconversion efficiencies ($\eta$).

Several groups have incorporated $Nb_2O_5$ in nanoparticles, nanobelts, fibers, and as coating layers for $TiO_2$ nanoparticles in DSSCs.[18] We report here, for the first time, construction of a $Nb_2O_5$ photoanode with the nanoforest structure and the results of investigations of the photoelectronic properties of this material under a variety of key growth parameters (layer thickness, background gas pressure and composition). We find that dye loading on these structures (and thus their surface area) increases with the pressure used during deposition, allowing fine control of the porosity of the structure. This is important because electron transport is highly dependent on the geometry of the three-dimensional network of particles. Increased porosity leads to decreased average coordination number and hence a higher number of "dead ends" (particles with only one neighbor), changing from 1% in a 50% porous film to 31% in a 75% porous film.[19] Furthermore, contrary to speculations regarding this nanoforest growth mode, the absolute background pressure does not play the determining role in developing the forest nanostructure. Rather, the key is the partial pressure of oxygen. Although no significant improvement in $V_{oc}$ was observed in tested devices, this nanostructure presents the largest photon-to-electron conversion efficiency yet observed for $Nb_2O_5$ as a photoanode in DSSCs: (~40%) with APCE ~90%. In addition, this pressure-controlled structure may open a path to a marriage of the best properties of random nanoparticle networks with oriented single-crystal nanotubes and rods.

## 2. EXPERIMENTAL SECTION

Photoanodes consisting of fluorine-doped tin oxide (FTO) glass coated with $Nb_2O_5$ were fabricated by pulsed laser deposition

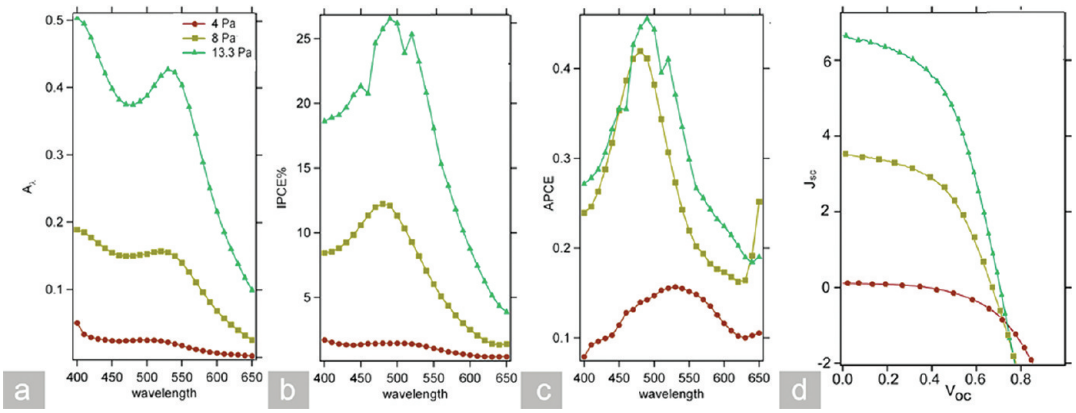


**Figure 3.** Photophysical characterization of films with $N_3$ dye deposited following treatment at different background oxygen pressures. (a) Absorbance values, (b) IPCE values, (c) APCE values, and (d) *IV* curves.

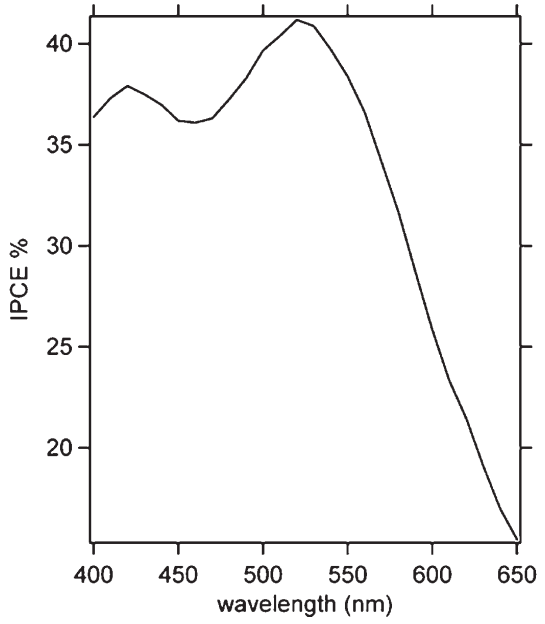


**Figure 4.** Enhanced IPCE for dye $N_3$ on $Nb_2O_5$ in 0.5MLiI with 0.05 M $I_2$. Film grown under 13.3 Pa oxygen pressure and 300k laser shots for a total 6 $\mu$m thickness.

(PLD) from a $Nb_2O_5$ target (from Kurt J Lesker, 99.9% purity) with a KrF excimer laser (248 nm, 300 mJ, 80 Hz) focused with a 60° incidence angle into the chamber and rastered over the target (pulse fluence 0.5 mJ/cm$^2$) The resulting plume was directed at FTO glass held 5 cm above the target. Both the target and the FTO substrate were continuously rotated at 40 and 20 rpm, respectively, for a uniform deposition. Prior to deposition, the PLD chamber was evacuated to a base pressure of $6 \times 10^{-6}$ Torr. PLD takes advantage of the high energy of the ablated species to allow film growth even at high gas background pressures, a feature not shared with other physical sputtering methods.[20] To systematically study the effect of PLD parameters on the morphological and photophysical performance of the $Nb_2O_5$ films, we varied oxygen pressure, partial oxygen pressure in a gas mix, and number of laser shots (which controls film thickness) with one parameter changing at a time. Because the columnar growth has been shown to be determined by the pressure of $O_2$ during deposition,[16] we initially performed a pressure variation study with a pure $O_2$ atmosphere. The oxygen pressure was varied from 4 to 13.3 Pa. To distinguish the pressure effect from chemical reactions involving oxygen, we varied the gas mix from purely Ar to a 1:1 mix of Ar and $O_2$ and again to pure oxygen. Finally, the thickness of the films was varied from ~30 nm (2k shots) to ~6 $\mu$m (300k shots). Following PLD growth, films were annealed at 500 C for one hour in air.

Morphological characteristics of these amorphous films were obtained by using a Hitachi S-4700 scanning electron microscope (SEM) and a JEOL 2010F transmission electron microscope (TEM). Both top-views and cross-sectional images of the films were obtained. Raman scattering (Dilor XY Triple spectrograph, liquid nitrogen cooled CCD detector, and 514.5 nm wavelength argon ion laser at 200 mW), X-ray photoelectron spectroscopy (XPS), and X-ray diffraction (Rigaku MultiFlex X-ray Diffractometer, Cu K$\alpha$ radiation, 40 kV-40 mA, scan speed: 4°/min) characterizations were used to confirm the formation of niobium oxide in the orthorhombic-$Nb_2O_5$ phase (Figure1). Derivatization of the PLD-$Nb_2O_5$/FTO films was achieved by soaking them in a $2 \times 10^{-4}$ M $Ru(dcbpyH)_2(NCS)_2$ (N3 dye) ethanol solution overnight. Surface dye loading was determined by UV−visible measurements incorporating an integrating sphere (Cary 5000 fitted with DRA 2500) to collect both reflectance and transmission spectra to calculate reflectance-corrected absorbance values. To make photophysical measurements, we fabricated a sealed sandwich cell (1 cm$^2$) by methods described by Z-S Wang et al,[21] with a 100 $\mu$m Surlyn spacer. The redox electrolyte used was 0.1 M LiI, 0.05 M $I_2$, 0.6 M dimethyl propyl imidazolium iodide, and 0.5 M tert-butylpyridine in dried acetonitrile. Incident photon-to-current efficiency (IPCE) values were obtained by using a 75W Xe Oriel 6251/Oriel Cornerstone 260 monochromator from which light was coupled through an optical fiber and made incident normal to the DSSC. Absorbed photon-to-current efficiencies (APCEs) were obtained by dividing IPCE by the fraction of light absorbed. Incident light intensity measurements were measured by using a calibrated Si-photodiode. Current measurements were conducted with a Keithley 6517A current meter. The current−voltage characteristics of the cells were measured with a Keithley 2400 source meter. An AM1.5 solar simulator (NEWPORT 1000-W Xe lamp and an AM1.5 filter) was employed as the light source for cell efficiency characterization.

## 3. RESULTS AND DISCUSSION

At oxygen background pressures of less than 4 Pa the PLD $Nb_2O_5$/FTO films obtained are dark and nontransparent with a stoichiometry of less oxygen than 2Nb:5O, as verified by XPS

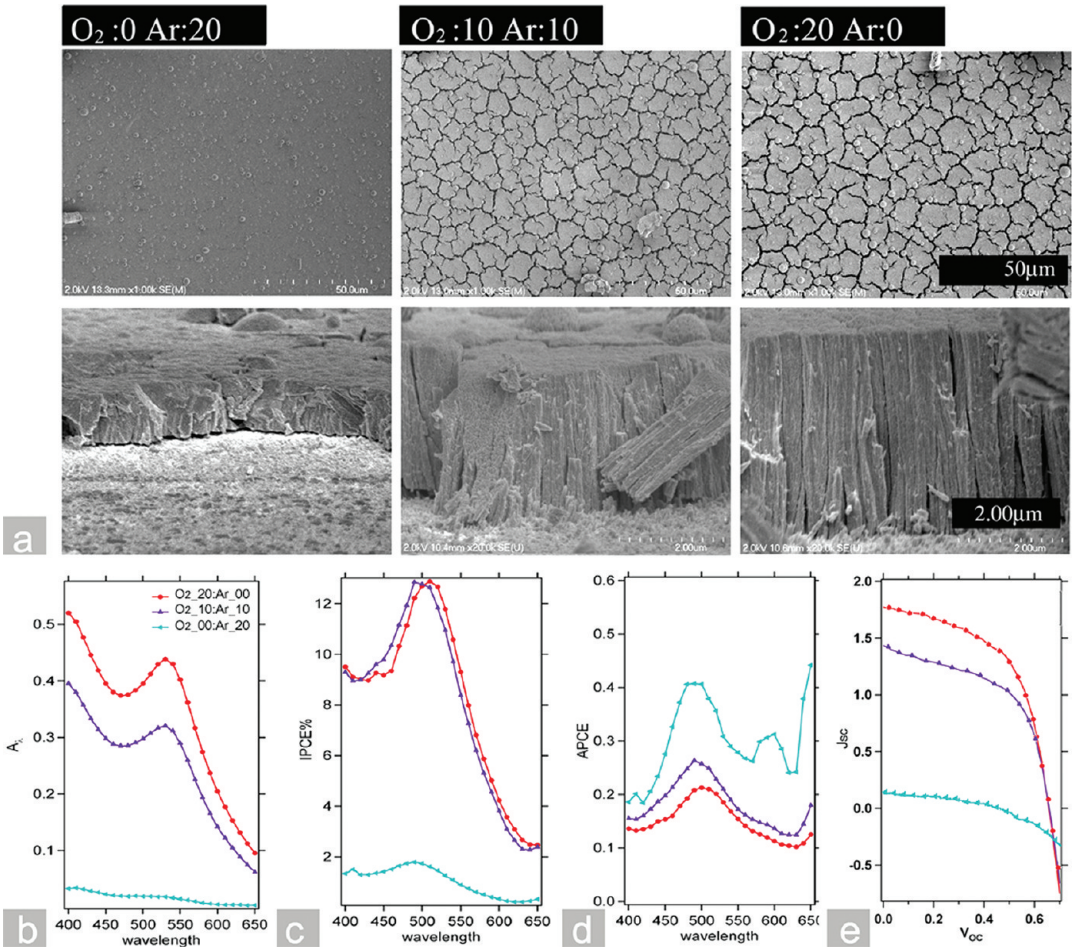


**Figure 5.** (a) Morphological and (b−d) photophysical characterization of films deposited in different gaseous environments. All films were prepared with 300k laser shots at an overall 10 Pa pressure.

analysis (not shown). Films deposited at background oxygen pressures at and just above 4 Pa are very compact and transparent but with very low porosity. Increasing the background oxygen pressure above 4 Pa led to a new deposition regime with increased porosity and segmentation of the film into a collection of domains made of separated oxide columns. The domains are separated by film fractures whose width spans a range of scales (see Figure 2) that depend upon the background gas pressure used during film growth. Cross-sectional views of films deposited at oxygen pressures between 7 and 15 Pa show that vertically aligned, ordered structures are the building blocks of the films (see in particular TEM images in Figure 2). Films fabricated with higher background oxygen pressure (not shown) reach an extreme in this growth mode resulting in morphologies similar to traditional nanoparticle films with very high porosity but disordered morphology.

The photophysical behavior of the films deposited under the different background oxygen pressures is shown in Figure 3. The light absorption due to dye loading for the 4 Pa film is very low, as expected for a compact film. At higher oxygen background pressures, the amount of dye loading and absorbed light increase due to the presence of individual nanoparticles which enhance the exposed surface area of the film. The presence of the film cracks (top view Figure 2) is observable at all deposition pressures. These fractures are a source of small but unwanted light scattering losses. The network of cracks could also play a role facilitating the electrolyte diffusion contrary to the standard nanoparticles sintered films, where the ions need to travel though tiny channels to move from the reservoir of the solution to the bottom of the oxide film. The nanoforest material offers a network of multiscale channels from the reservoir to a very close distance to each and every dye molecule. However, although there are significant crack density differences, the APCE curves for the 8 and 13.3 Pa films (Figure 2c) are very close to each other, suggesting their only significant dissimilarity is their dye loading capacity. The lower APCE for the 4 Pa film compared to nanoparticle based films at higher pressures is unexpected but may be due to poor electron transport or poor injection[22] caused by film defects that are a product of growth at the edge of the parameter range for 2Nb:5O stoichiometry. Similar trends are also observed for $J-V$ characteristics, including nearly linear increases in short circuit current ($J_{sc}$) and overall device efficiencies with increasing background oxygen pressures. The highest $V_{oc}$ of 710 mV and overall efficiency of 2.41% was observed for the 13.3 Pa film. These values are better[18,23] or comparable to those for the best niobia-based films[24] having similar area, thicknesses, and the same sensitizer. In order to probe the full potential of transport capabilities, we varied the electrolyte to 0.5 M LiI, 0.05 M $I_2$ in molecular sieve dried acetonitrile. Under these conditions, IPCE improved to 40% with >90% APCE,

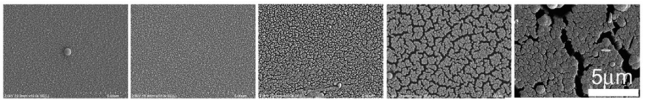


**Figure 6.** Top view of films with different thicknesses (from left to right: 2k, 10k, 20k, 60k, 300k laser shots). The increased height of the columns provides a larger torque for the increase in crack sizes.

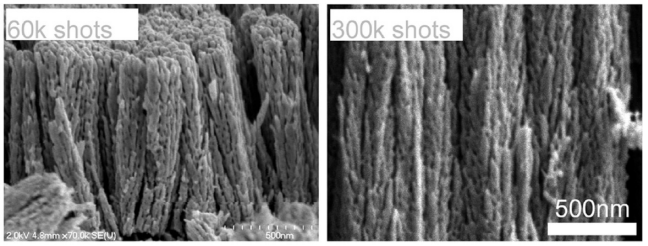


**Figure 7.** Cross-section images of films of different thicknesses controlled by the number of PLD shots. Morphology is largely thickness independent.

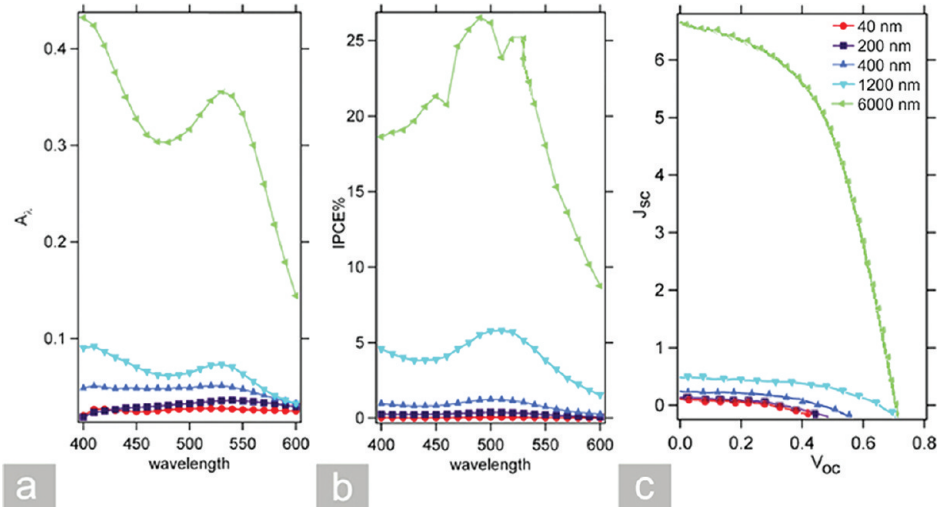


**Figure 8.** Photophysical characterization of films with different thicknesses show monotonic trends in absorbance, IPCE, and *JV* characteristics as function of film thickness.

**Table 1. Summary of Samples and Results**

| | oxygen pressure variation in pure $O_2$ and 300k laser shots | | | oxygen vs argon at constant pressure 10 Pa and 300k laser shots | | | thickness variation varying no. of laser shots at 13.3 Pa pure $O_2$ | | | | |
|---|---|---|---|---|---|---|---|---|---|---|---|
| experiments | 4 Pa | 8 Pa | 13.3 Pa | pure $O_2$ | Ar/$O_2$ mix | pure Ar | 300k | 60k | 20k | 10k | 2k |
| optical density at wavelength 534 nm | 0.02 | 0.15 | 0.46 | 0.44 | 0.32 | 0.02 | 0.41 | 0.07 | 0.03 | | |
| thickness ($\mu$m) | 5.1 | 5.2 | 5.9 | 5.1 | 3.5 | 1.1 | 6.1 | 1.2 | 0.4 | 0.2 | 0.04 |
| N3 dye loading ($\times 10^{20}$ molecules/cm$^3$) | 0.017 | 0.130 | 0.328 | 0.363 | 0.385 | 0.077 | 0.283 | 0.262 | 0.320 | | |
| max. IPCE value (%) | 1.41 | 12.2 | 27.7 | 12.8 | 12.8 | 1.7 | 25.3 | 5.7 | 1.1 | 0.36 | 0.06 |
| $V_{oc}$ (V) | 0.37 | 0.66 | 0.71 | 0.65 | 0.66 | 0.45 | 0.71 | 0.65 | 0.47 | 0.33 | 0.29 |
| $J_{sc}$ (mA/cm$^2$) | 0.106 | 3.53 | 6.65 | 1.76 | 1.43 | 0.14 | 6.65 | 0.48 | 0.23 | 0.136 | 0.101 |
| fill factor (%) | 44 | 50.6 | 49 | 57 | 54 | 40 | 50 | 50 | 48 | 43 | 47 |
| efficiency (%) at 1 sun | 0.17 | 1.17 | 2.41 | 0.65 | 0.51 | 0.02 | 2.3 | 0.16 | 0.05 | 0.02 | 0.01 |

which is the highest value reported for niobia prepared by any method (Figure 4). Koops[22] and Wu[25] observed similar photocurrent increases in $TiO_2$ devices with the increased concentration of Li+ ions and absence of tert-butylpyridine, an effect

which they conclude is due to the downward shift of the $TiO_2$ conduction band because of the intercalation by the high charge density Li+ ions.

To investigate the effect of gas composition on the growth of the columnar structures, the composition of the background gas was varied from pure argon to pure oxygen keeping the total background pressure constant at 10 Pa. It is obvious from the SEM micrographs shown in Figure 5a that films prepared with no oxygen present during deposition are extremely compact and relatively crack free, similar to films grown at 4 Pa of pure oxygen. The situation is completely different in the presence of an oxygen background. Both cross-sectional and top views of films prepared in 50% Ar:50% $O_2$ and in pure oxygen show that those conditions result in similar crack and island dimensions, as well as columnar structures. Thus, one can conclude that some amount of background oxygen is needed to enable the forest growth, and the overall pressure required can be supplied by an inert component. After annealing in air, all traces of the background mix used during fabrication are likely to be removed and XPS studies show similar stoichiometry for all films. Photophysical studies with the $N_3$ dye (Figure 5b−e) show that light absorbance, IPCE, APCE, and $J-V$ curves (all done in dried CH3CN with 0.1 M LiI, 0.05 M $I_2$, 0.6 M dimethyl propyl imidazolium iodide, and 0.5 M tert-butylpyridine) are similar for the mixed gas and pure oxygen films but very different for the film made in pure Argon. These observations point to the nanostructure as the dictating factor for photophysical activity in these films.

A thickness dependence study was conducted by controlling the number of pulse shots (2k- 300k shots) used for deposition (in 13.3 Pa of pure oxygen background). Film thicknesses were varied from 40 to 6 $\mu$m. The top views (Figure 6) of films with different thicknesses show differences in the bundle sizes as well as dimensions of the cracks. The widening of existing cracks, as observed in the top view, happens during annealing due to the increased stress during FTO- niobia bonding and, perhaps, due to the mismatch in thermal expansion coefficients between materials. This structural motif is similar to that observed in wetting−dewetting experiments for $TiO_2$ PLD grown films immersed in water and ethanol.[26] Figure 7 shows that the thickness does not affect the nature of the vertical growth and the nanoforest structure appears the same independent of the number of laser shots. IPCE and JV curves are shown in Figure 8 and they show improved device performance with increased thickness (because of higher light absorption, also shown in Figure 8), as expected. However, we found it difficult to calculate APCE values based on the low light absorption of the thinnest films.

## 4. CONCLUSIONS

We have investigated conditions for growth of $Nb_2O_5$ "nanoforest" films by using laser ablation. Films were deposited at different background pressures, gas environments and with different thicknesses, and all of them have been characterized as DSSC photoanodes. Their behavior is summarized in Table 1. We found that, like Grätzel's $TiO_2$ nanoforest, $Nb_2O_5$ grows in a similar vertically aligned nanocrystalline structure under pressure-controlled pulsed laser deposition. However, this growth mode is not defined uniquely by the background pressure under deposition. We have shown that a partial pressure of oxygen is needed to develop it. Similar structures were obtained for pure oxygen and 50:50 oxygen:argon environments, both very different from films deposited in a pure argon atmosphere. The nanoparticle bundles present monotonic improvement in dye loading (4th row Table 1) and concomitant device performance as function of growth oxygen pressure and thickness. From the known absorbance cross section of the N3 dye molecules ($1.42 \times 10^7$ $cm^2$ $mol^{-1}$ at wavelength 534 nm[23]), the best PLD $Nb_2O_5$ films load N3 dye molecules with a 0.3 to 0.4 $\times$ $10^{20}$ molecules/$cm^3$ density, which is a factor 3−4 lower than a champion $TiO_2$ cell but also 1−5 times better than previously reported $Nb_2O_5$ photoanodes.[18,23,24] Besides some optical losses, the density and size of the film cracks do not appear to present a detrimental effect in the devices. Our results reveal the importance of pressure and gas composition during deposition. This work supports that this interesting morphology is independent to great extent of the material. So in addition to $Nb_2O_5$, other oxide candidates for photoanodes with high conduction band levels such as $Ta_2O_5$ and $SrTiO_3$ are likely to grow in similar fashion, allowing their deposition in layers and doping combinations previously difficult or impossible with traditional sol−gel approaches.

## AUTHOR INFORMATION

**Corresponding Author**
*E-mail: rln@physics.unc.edu.

## ACKNOWLEDGMENT

This material is based upon work wholly supported as part of the UNC EFRC: Solar Fuels and Next Generation Photovoltaics, an Energy Frontier Research Center funded by the U.S. Department of Energy, Office of Science, Office of Basic Energy Sciences under Award DE-SC0001011.

## REFERENCES

(1) Wadia, C.; Alivisatos, a P.; Kammen, D. M. *Environ. Sci. Technol.* **2009**, *43*, 2072–2077.
(2) O'Regan, B.; Gratzel, M. *Nature* **1991**, *353*, 737–740.
(3) Chen, C.-Y.; Wang, M.; Li, J.-Y.; Pootrakulchote, N.; Alibabaei, L.; Ngoc-le, C.-H.; Decoppet, J.-D.; Tsai, J.-H.; Gratzel, C.; Wu, C.-G.; Zakeeruddin, S. M.; Graetzel, M. *ACS Nano* **2009**, *3* (10), 3103–3109.
(4) Frank, A. J.; Kopidakis, N.; van de Lagemaat, J. *Coord. Chem. Rev.* **2004**, *248*, 1165–1179.
(5) Kong, F.-T.; Dai, S.-Y.; Wang, K.-J. *Adv. Optoelectronics* **2007**, 1–14.
(6) Wei, D. *Int. J. Mol. Sci.* **2010**, *11*, 1103–1113.
(7) Wurfel, U.; Peters, M.; Hinsch, A. *J. Phys. Chem. C* **2008**, *112*, 1711–1720.
(8) Vayssieres, L.; Keis, K.; Hagfeldt, A.; Lindquist, S.-E. *Chem. Mater.* **2001**, *13*, 4395–4398.
(9) van de Lagemaat, J.; Frank, A. J. *J. Phys. Chem. B* **2001**, *105*, 11194–11205.
(10) Leng, W. H.; Barnes, P. R. F.; Juozapavicius, M.; O'Regan, B. C.; Durrant, J. R. *J. Phys. Chem. Lett.* **2010**, *1*, 967–972.
(11) Archana, P. S.; Jose, R.; Vijila, C.; Ramakrishna, S. *J. Phys. Chem. C.* **2009**, *113*, 21538–21542.
(12) Varghese, K. O.; Paulose, M.; Grimes, C. A. *Nat. Nanotechnol.* **2009**, *4*, 592–7.
(13) Sauvage, F.; Di Fonzo, F.; Li Bassi, A.; Casari, C. S.; Russo, V.; Divitini, G.; Ducati, C.; Bottani, C. E.; Comte, P.; Graetzel, M. *Nano Lett.* **2010**, *10* (7), 2562–7.
(14) Graetzel, M. *J. Photochem. Photobiol., C* **2003**, *4* (2), 145–153.
(15) Jose, R.; Thavasi, V.; Ramakrishna, S. *J. Am. Chem. Soc.* **2009**, *92* (2), 289–301.

(16) Feng, X.; Shankar, K.; Paulose, M.; Grimes, C. A. *Angew. Chem., Int. Ed.* **2009**, *48* (43), 8095–8.
(17) Grimes, C. A.; Varghese, O. K.; Ranjan, S. *Light, Water, Hydrogen—The Solar Generation of Hydrogen by Water Photoelectrolysis*; Springer: New York, 2007; pp 191—255.
(18) Viet, A. L.; Jose, R.; Reddy, M. V.; Chowdari, B. V. R.; Ramakrishna, S. *J. Phys. Chem. C* **2010**, 21795–21800.
(19) Benkstein, K. D.; Kopidakis, N.; van de Lagemaat, J.; Frank, A. J. *J. Phys. Chem. B* **2003**, *107* (31), 7759–7767.
(20) Hubler, G. K. *Pulsed Laser Deposition of This Films*; John Wiley & Sons: New York, 1994; pp 327—354.
(21) Wang, Z. *Coord. Chem. Rev.* **2004**, *248*, 1381–1389.
(22) Koops, S. E.; ÒRegan, B. C.; Barnes, P. R. F.; Durrant, J. R. *J. Am. Chem. Soc.* **2009**, *131*, 4808–4818.
(23) Sayama, K.; Sugihara, H.; Arakawa, H. *Chem. Mater.* **1998**, *10* (12), 3825–3832.
(24) Guo, P. *Thin Solid Films* **1999**, *351* (1—2), 290–294.
(25) Wu, J.; Lan, Z.; Hao, S.; Li, P.; Lin, J.; Huang, M.; Fang, L.; Huang, Y. *Pure Appl. Chem.* **2008**, *80* (11), 2241–2258.
(26) Fusi, M.; Di Fonzo, F.; Casari, C. S.; Maccallini, E.; Caruso, T.; Agostino, R. G.; Bottani, E.; Li Bassi, A. *Langmuir* **2011**, *27* (18), 1935–1941.